MATERIALS PHYSICS AND MECHANICS RESEARCH ARTICLE

Submitted: February 24, 2026 **Revised: April 13, 2026** **Accepted: April 27, 2026**

EBSD study of microstructure produced during laser powder bed fusion of 17-4 PH martensitic steel

I.S. Nikitin [1], E.A. Voropaeva [1], A.O. Semenyuk [1], R.S. Chernichenko [1], P.D. Dolzhenko [1], S.I. Borisov[1], A.A. Kalinenko [1], E.V. Kaliuzhnaya [1], I.S. Zuiko [1], L. Shi [2], C. Wu [2], S.Yu. Mironov [1] ✉

[1] Belgorod National Research University, Belgorod, Russia

[2] Shandong University, Jinan, China

✉ mironov@bsuedu.ru

ABSTRACT

Electron backscatter diffraction was applied to investigate the broad aspects of the microstructure produced during laser powder beam fusion of 17-4 PH steel. It was found that the laser powder beam fusion process involved the δ-ferrite-to-austenite-to-martensite phase transformation sequence. Remarkably, the solidification <100> + <111> fiber texture in δ-ferrite was essentially inherited by the final martensitic phase, i.e., the texture-memory effect was observed. It was also revealed that the δ-ferrite-to-austenite transformation involved a strict selection of crystallographic variants. This led to a pronounced crystallographic preference of 60° <111> boundaries in the austenitic phase. The core result of this study was an integral pattern of microstructural changes during laser powder beam fusion from a solidification stage down to ambient conditions.

KEYWORDS

martensitic steels • laser powder bed fusion • electron backscatter diffraction • microstructure • texture

Funding. *The work was supported by the government assignment FZWG-2026-0005 "Development of scientific foundations for optimization of selective laser melting and subsequent heat treatment of precipitation-hardening martensitic steel 17-4 PH", Ministry of Science and Higher Education of the Russian Federation.*

Citation: Nikitin IS, Voropaeva EA, Semenyuk AO, Chernichenko RS, Dolzhenko PD, Borisov SI, Kalinenko AA, Kaliuzhnaya EV, Zuiko IS, Shi L, Wu C, Mironov SYu. EBSD study of microstructure produced during laser powder bed fusion of 17-4 PH martensitic steel. *Materials Physics and Mechanics.* 2026;54(3): 1–19. http://dx.doi.org/10.18149/MPM.5432026_1

Introduction

Due to its optimal combination of strength and corrosion resistance across a broad temperature range, 17-4 PH martensitic steel is extensively utilized in the aerospace, petrochemical, and marine sectors. Furthermore, a recent innovation in additive laser powder bed fusion (L-PFB) technology may expand the applicability of this material for the production of complex-shaped parts.

The L-PBF technology involves the incremental, layer-by-layer melting and fusion of atomized metal powder using a laser beam following an appropriate computer model [1,2]. Owing to the unique characteristics of the L-PBF process, the manufactured material experiences a non-trivial thermal history, which involves an extremely high cooling rate (~10^6 K/s) and a pronounced thermal cycling, including several melting-to-solidification

© I.S. Nikitin, E.A. Voropaeva, A.O. Semenyuk, R.S. Chernichenko, P.D. Dolzhenko, S.I. Borisov, A.A. Kalinenko, E.V. Kaliuzhnaya, I.S. Zuiko, L. Shi, C. Wu, S.Yu. Mironov, 2026.
Publisher: Peter the Great St. Petersburg Polytechnic University
This is an open access article under the CC BY-NC 4.0 license (https://creativecommons.org/li-censes/by-nc/4.0/)

events. In the 17-4 PH martensitic steel, L-PBF typically results in intricate microstructures. Those may exert an essential influence on service properties of the L-PBFed parts, and therefore a fundamental understanding of the underlying microstructural mechanisms is necessary. Accordingly, this issue attracts considerable research interest.

It is well established that the L-PBFed parts normally exhibit a specific *meso-scale* structure that is often referred to as either "local molten pools" or "fish scale" patterns. This structure is usually attributed to a localized nature of melting and subsequent solidification of initial powder material during L-PBF. Quite often, the transverse size of the local molten pools is comparable with the width of the laser beam.

Within the local molten pools, a complex mixture of δ-ferrite, austenite, and martensite is often found [3–33]. The preservation of the δ-ferrite in the microstructure is usually explained by the extremely high cooling rate [12,34–36], while the nucleation of the austenite-martensite structure is sometimes related to thermal cycling [32–34], which are both inherent to L-PBF. Remarkably, the proportions of the phases may vary over a wide range, depending on the nature of the powder material and conditions of L-PBF.

Typically, the δ-ferrite preferentially concentrates in the central parts of the local molten pools, while the austenitic and martensitic phases tend to cluster at their periphery [20,32,33,37–39]. This latter effect was most likely related to the inhomogeneous character of thermal cycling, which is most pronounced in these areas. On the other hand, at the micro-scale structural level, the austenite often precipitates along the δ-ferrite grain boundaries [20,32,33,37,39–43]. With an increase in the volume fraction, the austenitic phase tends to propagate in the interior of the δ-ferrite grains, producing a Widmanstatten structure [20,39].

Normally, the δ-ferrite phase exhibits a distinct dendritic morphology, thus suggesting its solidification from a melt. It is believed that this phase nucleates epitaxially at the borders of the local molten pools and then grows in a heat flow direction [12,23,34,44]. The growing δ-ferrite dendrites are often observed to penetrate through multiple additive layers [5,12,17,23,34,37,41,45]. This finding is consistent with the presumed epitaxial nucleation mechanism of this phase, according to which the freshly nucleated grain inherits the crystallographic orientation of a substrate additive layer [5,23,27,34,35]. An increase in the volumetric energy density during L-PBF may result in an abnormal coarsening of the dendrite structure [37,43]. Sometimes, the rapidly growing dendrites may completely consume their parent molten pool area, thus giving rise to a characteristic "mosaic" structure [37,42]. Moreover, this may also enhance the interlayer growth of the dendrites [37,46].

As a rule, the δ-ferrite phase shows a pronounced <100> fiber texture [3,10,23,47–51], which is normally expected to develop during solidification of cubic metals. Remarkably, the fiber texture may be aligned not only with the building direction of the L-PBF but also with a laser scanning direction (or even directions) [20,37,43]. This observation suggests a complex nature of thermal fields generated within the local molten pools. In some cases, such an integral textural pattern may be close to the {001}<100> cube texture [37,43].

In comparison with the δ-ferrite, the microstructural characteristics of the evolved austenitic and martensitic phases are much less studied. Nevertheless, it has been shown that all three phases may be related to each other via either the Kurdjumov-Sachs [20,32] or Nishiyama-Wassermann [32,42] orientation relationships. Another remarkable issue is

also the fine-grained nature of the austenite [20,32]. It is sometimes believed that this factor may hinder or even suppress the martensitic transformation in the L-PBFed material [39,44]. The textures produced in the austenitic and martensitic phases are usually poorly developed [20,52]. Nevertheless, a <110> fiber texture has been found in austenite [4,10,32,48], while a <111> fiber texture may develop in the martensite [10,48].

The above works have provided a valuable insight into the microstructural aspects of the L-PBF of 17-4 PH martensitic steel. Nevertheless, given the complex character of the involved microstructural phenomena, the *integral* pattern of microstructural processes in all three phases is still lacking. The present study attempted to bridge this gap in our knowledge. To this end, the microstructural characteristics of δ-ferrite, austenite, and martensite were consistently examined using the advanced electron backscatter diffraction (EBSD) technique.

Materials and Methods

The program material for this work was a commercial 17-4 PH martensitic steel with the nominal chemical composition listed in Table 1. The material was produced by 3D Systems Inc. utilizing a nitrogen-gas atomization process and supplied as an atomized metallic powder. The powder particles had a nearly spherical shape and often incorporated satellites. The particle size ranged from 1.4 to 53.2 μm, with a mean volume diameter being 13.5 μm. The percentile diameters were D_{10} ≈ 4.2 μm, D_{50} ≈ 11.5 μm, and D_{90} ≈ 25.8 μm.

Table 1. Nominal chemical composition of 17-4 PH martensitic steel (wt. %)

Fe	Cr	Ni	Cu	Mn	Si	Ta + Nb	C	P	S
Balance	15.0–17.5	3.0–5.0	3.0–5.0	⩽ 1.0	⩽ 1.0	0.15–0.45	⩽ 0.07	⩽ 0.04	⩽ 0.03

The LPBF process was performed on a ProX DMD 200 machine (3D Systems). It is important to emphasize that the present study was a part of a wide-ranging research project, which aimed to elucidate the broad aspects of the microstructures produced during LPBF. A series of preliminary experiments showed that all additive materials

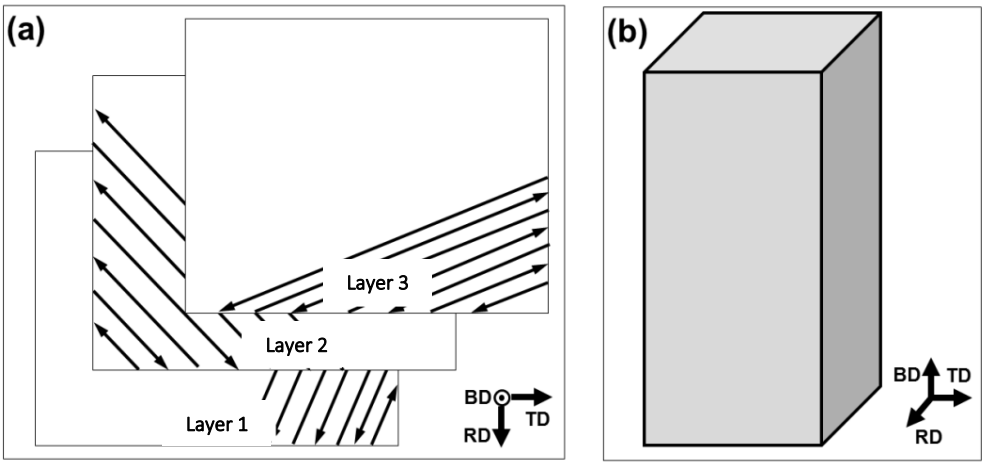


Fig. 1. Schematics showing (a) the applied strategy of 3D printing (i.e., 67-degree rotation of laser beam) and (b) the built sample. BD, RD, and TD define the building direction, the motion direction of the powder roller, and the transverse direction, respectively

exhibited virtually the same phase composition (i.e., δ-ferrite, austenite, and martensite), while the variation in LPBF conditions provided only a change in the phase ratio. Accordingly, a more or less typical example was selected for a detailed investigation of the phase microstructures in the present study. In this particular case, L-PBF variables were adjusted to provide a relatively high volumetric energy density with the aim to minimize retained porosity. These included a laser power of 150 W, a laser scanning speed of 0.5 m/s, a hatch distance of 50 μm, and a powder layer thickness of 30 μm, resulting in a volumetric energy density of 200 J/mm^3. A cuboidal sample measuring 20 × 10 × 70 mm^3 was built in a nitrogen atmosphere. A simple parallel scan strategy was employed with the laser scan direction rotated by 67° between successive layers (Fig. 1(a)). A typical L-PBF geometry was adopted in this work, i.e., the building direction (BD), the motion direction of the powder roller (RD), and the transverse direction (TD), as shown in Fig. 1(b).

Microstructural observations were performed by EBSD. For the examinations, the built sample was sectioned in half along the building direction, mounted into a conductive resin, and mechanically polished using standard metallographic procedures. A final surface finish was attained using ≈ 12-h vibratory polishing with an OP-S colloidal silica suspension.

EBSD analysis was performed employing an FEI Quanta 600 field-emission-gun scanning electron microscope (FEG-SEM) equipped with TSL OIM™ software and operated at an accelerated voltage of 20 kV. Microstructural observations were focused on the central part of the built sample. To provide both a necessary spatial resolution and sufficient sampling statistics, an intermediate EBSD scan step size of 0.5 μm was applied. Considering the difficulty of discriminating ferrite from martensite in EBSD, these two were both indexed as the preset iron-alpha phase of the EBSD software. To enhance the reliability of EBSD data, the fine grains comprising two or one pixel were automatically "cleaned" from the acquired EBSD map using the standard grain-dilation option of EBSD software. To eliminate spurious boundaries caused by orientation noise, a lower limit boundary misorientation cut-off of 2° was applied. A 15° criterion was used to differentiate low-angle boundaries (LABs) from high-angle boundaries (HABs). Grain size measurements were performed employing the grain-reconstruction method [53], according to which the measured grain area in the EBSD map was converted into the circle-equivalent diameter.

The particular EBSD characteristic, the image quality (IQ) index (which is sometimes referred to as the pattern quality or band contrast index), was used for microstructural analysis. The IQ index characterizes the sharpness of the Kikuchi bands in a digitized diffraction pattern and serves as a qualitative measure of stored energy.

Results and Discussion

Broad aspects of evolved structure

The EBSD IQ map of a typical microstructure that evolved in the central part of the built sample is shown in Fig. 2(a). A selected area of the map is given at higher magnification in Fig. 2(b). In the map, the austenitic phase is highlighted with red, while the δ-ferrite/martensite structure is shown in gray.

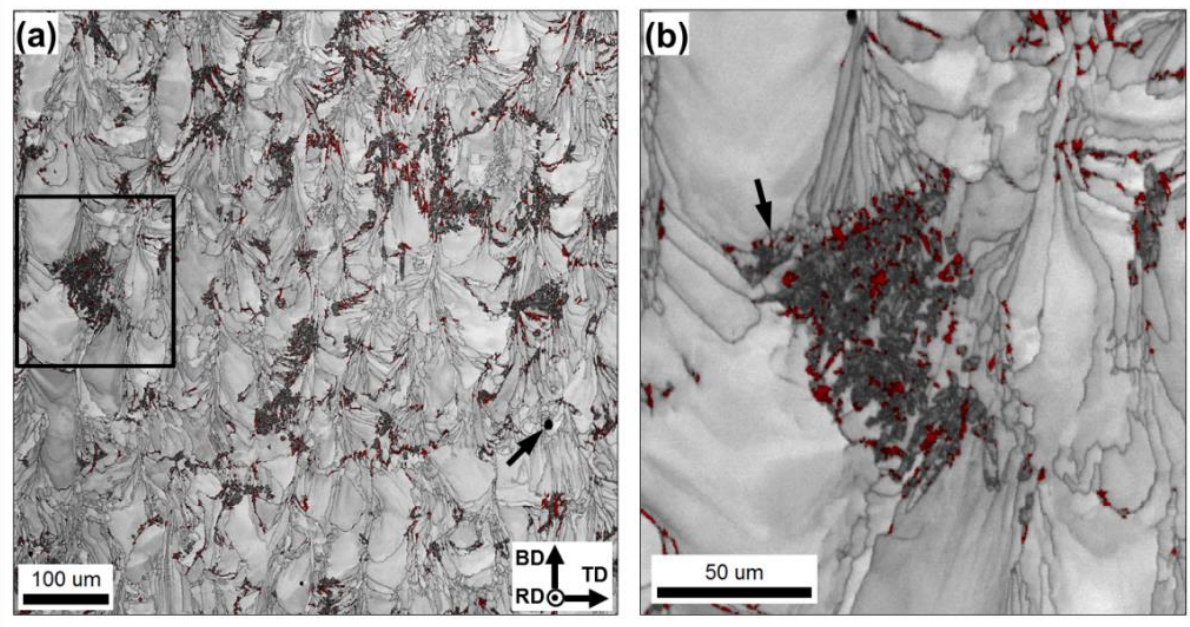


Fig. 2. (a) EBSD image-quality map of produced microstructure (austenitic phase is highlighted with red) with selected area shown at higher magnification in (b). In (a), the arrow exemplifies the retained gas porosity. In (b), the arrow shows the fine-grained δ-ferrite structure near the local molten pool border. BD, RD, and TD define the building direction, the motion direction of the powder roller, and the transverse direction, respectively

Despite the additive sample being built at a relatively high energy density, a minor fraction of nearly spherical discontinuities was still found in the material (an example is arrowed in Fig. 2(a)). Those presumably represented residual gas porosity.

A distinct "fish scale" structure was revealed in the EBSD map (Fig. 2(a)). As noted in the Introduction section, this meso-scale structure is characteristic of the L-PBFed parts and arises from the localized character of the melting-to-solidification sequence during the additive manufacturing process. In accordance with expectations, the typical breadth of the local molten pools was ~ 100 μm, i.e., it was comparable with the width of the laser beam applied in the present study (≈ 78 μm).

On the other hand, the characteristic depth of the pools was also ~ 100 μm in size (Fig. 2(a)), i.e., it significantly exceeded the nominal thickness of the powder layer (i.e., 30 μm). This discrepancy is often reported in the scientific literature [54], where it is explained in terms of the so-called "effective" thickness of the powder layer. Briefly, the density of the powder material is considerably lower than the density of a parent solid material. Hence, the solidification of the molten powder material should result in a volume reduction. Accordingly, the "effective" thickness of the next deposited powder layer should be greater than the nominal thickness, which is preset in the L-PBF system. An alternative explanation for the revealed discrepancy may also be a relatively deep depth of the local molten pools due to the high energy density applied in the present study (i.e., 200 J/mm^3). In this case, the local material may experience several melting-to-solidification cycles during the L-PBF process.

Quite expectedly, the microstructure distribution within the local molten pools was inhomogeneous (Fig. 2(a)). Specifically, the central part of the pools was typically occupied by the comparatively coarse, columnar-shaped grains, which presumably represented the δ-ferrite phase. Conversely, the fine-grained austenite/martensite structure tended

to cluster near the pool borders, preferentially at the pool triple joints, as exemplified in Fig. 2(b). This observation agreed well with the scientific literature [20,32,33,37–39] and suggested fairly inhomogeneous temperature distribution during the L-PBF process.

A remarkable issue was also the formation of the fine equiaxed grains at the borders of the local molten pools (an example is arrowed in Fig. 2(b)). Considering their morphology, those likely represented δ-ferrite rather than martensite. If so, the fine-grained structure may be attributable to either the particularly high cooling rate on the solidification surface or a static recrystallization presumably occurring during thermal cycling.

Microstructure partitioning

As mentioned in the previous section, the reliable discrimination between ferrite and martensite in EBSD is challenging. This problem arises from a relatively small difference in the crystallography between these two phases, which is hard to resolve by EBSD. To overcome this difficulty, several approaches have been proposed in the scientific literature. One of the most common methods is based on the concept of the principal difference in stored energy between the ferrite and martensite [32,33,55–63]. Hence, the distribution of the related EBSD characteristics (typically, the IQ index) should exhibit a transition from one phase to another.

In the IQ EBSD map shown in Fig. 2(a), two distinct microstructural constituents could be recognized, viz., (i) the coarse-grained columnar structure with a comparatively bright IQ contrast (i.e., the low stored energy) and (ii) the fine-grained component with a darker IQ contrast (i.e., a higher stored energy). From the above characteristics, it was likely that the former constituent represented δ-ferrite, while the latter one was martensite.

The distribution of the grain average IQ index derived from the above-mentioned EBSD map is presented in Fig. 3(a). The distribution exhibited a clear asymmetry consisting of a narrow central peak, a broad maximum in the high IQ range, and an extreme end ("a tail") in the low IQ interval. From the broad perspective, it was likely that these three constituents represented martensite, δ-ferrite, and retained porosity, respectively. Importantly, the transitions between the constituents were smooth, and no clear threshold was found.

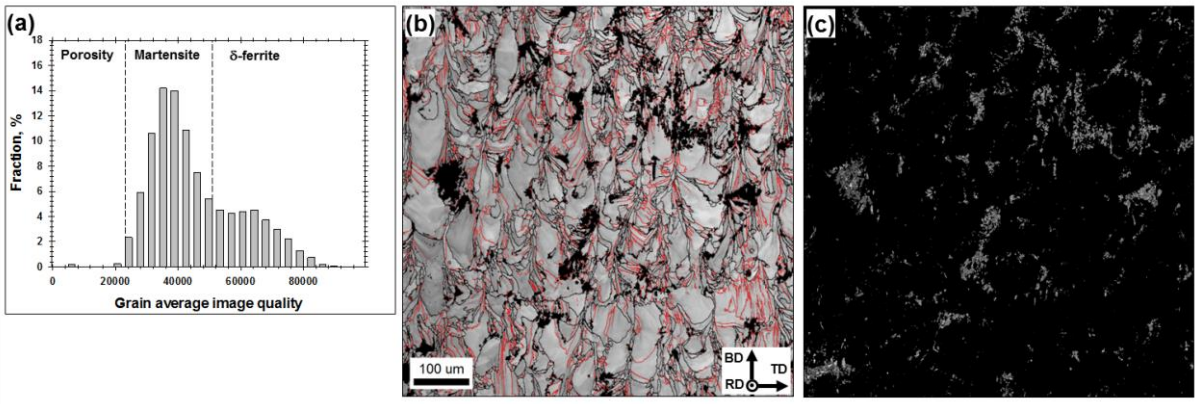


Fig. 3. Partitioning of δ-ferrite/martensite structure: (a) distribution of the grain average image-quality index, (b) partitioned δ-ferrite, and (c) partitioned martensite. In (a), the presumed transitions from porosity to martensite and then to δ-ferrite are shown. In (b), red lines show low-angle boundaries in δ-ferrite. Note: the common scale bar and reference frame for (b) and (c) are indicated (b); BD, RD, and TD define the building direction, the motion direction of the powder roller, and the transverse direction, respectively

Using a trial-and-error approach, the approximate thresholds between the porosity, martensite, and δ-ferrite were defined at IQ = 24,255 and IQ = 53,000. For clarity, the presumed borderlines between the constituents were indicated by dotted lines in Fig. 3(a). Based on these thresholds, the experimental IQ map in Fig. 2(a) was partitioned into δ-ferrite and martensite components, as shown in Fig. 3(b,c), respectively. It was found that the data points with a relatively high IQ index (IQ ⩾ 53,000) encompassed all coarse columnar-shaped grains (Fig. 3(b)). Remarkably, the observations of the grains using transmission-electron microscopy (TEM) revealed no lath-shaped microstructural elements (not shown). It is likely, therefore, that these represented the δ-ferritic phase. On the other hand, the pixels in the range of 24,255 ⩽ IQ < 53,000 were arranged as a fine-grained structure (Fig. 3(c)), thereby presumably representing the martensitic phase. The reasonable agreement between the IQ distribution (Fig. 3(a)) and the morphology of the partitioned microstructures (Fig. 3(b,c)) suggested the reliability of the employed approach.

Thus, in agreement with the scientific literature [3–33], the produced microstructure represented a complex mixture of δ-ferrite, austenite, and martensite. Assuming that the microstructural evolution during L-PBF involved the δ-ferrite-to-austenite-to-martensite phase transformation sequence, the detailed microstructural characterization of each phase may shed light on this process. Accordingly, the microstructures evolved in these phases were considered hereafter.

Microstructure of δ-ferrite

The EBSD IQ map of the δ-ferrite microstructure is shown in Fig. 3(b). In the map, LABs and HABs are depicted as red and black lines, respectively. The grain-size distribution derived from the map is given in Fig. 4(a). The EBSD map clearly indicated that the material produced by L-PBF was predominantly composed of δ-ferrite, with a measured volume fraction of ≈ 89.4 %. The dominance of this metastable phase evidenced the extremely high cooling rate during L-PBF, in broad accordance with the scientific literature.

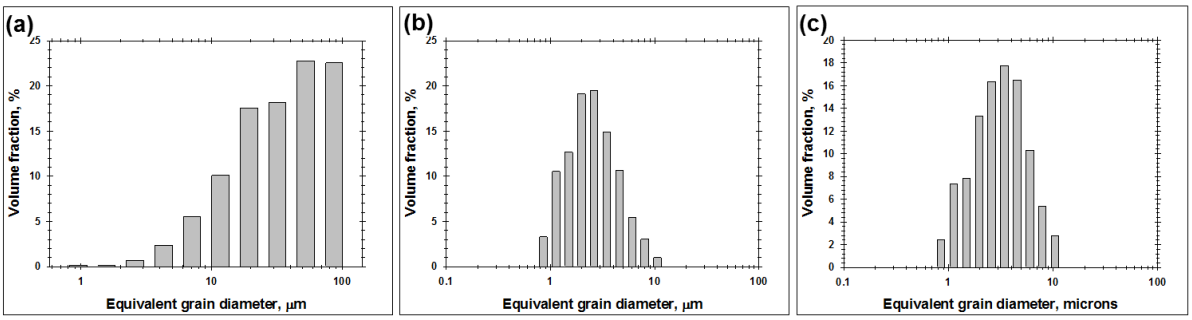


Fig. 4. Grain size distributions in (a) δ-ferrite, (b) austenite, and (c) martensite

Importantly, the median grain size of the δ-ferrite was close to ~ 100 μm (Fig. 4(a)), and therefore, it was comparable with a characteristic dimension of the local molten pools. Accordingly, the pools often had a nearly single crystal structure (Fig. 3(b)). On the other hand, the grain-size distribution also exhibited a pronounced extreme end in the fine-grain range (Fig. 4(a)). This observation reflected the fine-grained structure revealed at the molten pool borders, as exemplified in Fig. 2(b) (arrow).

It was also noteworthy that the δ-ferrite dendrites contained a developed LAB substructure (Fig. 3(b)), the fraction of which consisted of 45 % of the total measured grain-boundary area. Remarkably, the LABs were often arranged as nearly parallel sets of boundaries, which extended across entire δ-ferrite grains. It may be suggested, therefore, that the LASBs outlined individual dendrites. If so, these boundaries may originate from the orientation pinning effect, i.e., the mutual impingement of the growing dendrites with close crystallographic orientations.

To investigate crystallographic texture in δ-ferrite, orientation data were derived from the EBSD map in Fig. 3(b) and arranged as 100, 111, and 110 pole figures in Fig. 5(a,b,c), respectively. The reference frame for all pole figures was indicated in the bottom right corner.

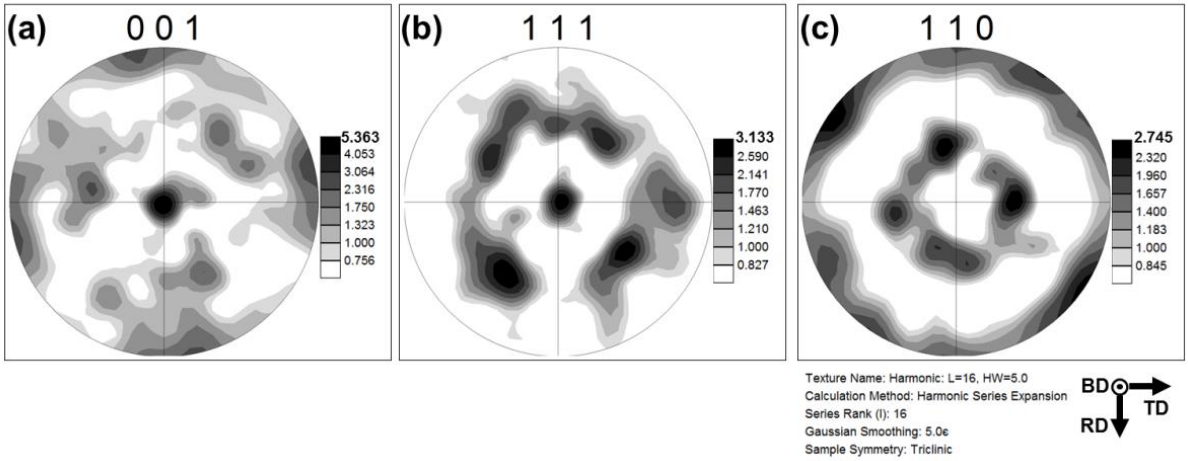


Fig. 5. Pole figures (a) 100, (b) 111, and (c) 110 showing crystallographic texture in δ-ferrite. Note: the reference frame for all pole figures is given in the bottom right corner. BD, RD, and TD define the building direction, the motion direction of the powder roller, and the transverse direction, respectively

Considering the limited statistics of sampled grains in the EBSD map in Fig. 2(a) (and the concomitant experimental scattering), the produced textural pattern could be interpreted in terms of a two-component <100> + <111> fiber texture, with both fibers being aligned with the building direction (Fig. 5(a,b)). The <100> fiber is typically revealed in the L-PBFed of 17-4 PH martensitic steel [3,10,23,47–51], and therefore this finding aligns well with the scientific literature. On the other hand, the formation of the <111> fiber was rather surprising.

According to Pirgazi et al. [64], this phenomenon can be explained by the specific temperature fields generated within the local molten pools when employing a 67° rotation strategy during laser scanning, as utilized in the current study. In this case, the steepest temperature gradient within a melt pool lies nearly perpendicular to the side surface, which, in turn, was the axis of a preferential dendrite growth. Assuming a 45-degree inclination of the poolside surface, the <100> orientation of the growing dendrites should produce a nearly <111> texture along the building direction.

To provide additional insight into the δ-ferrite microstructure, misorientation distribution was examined, as shown in Fig. 6. In accordance with expectations, the distribution exhibited a pronounced low-angle maximum, thus reflecting

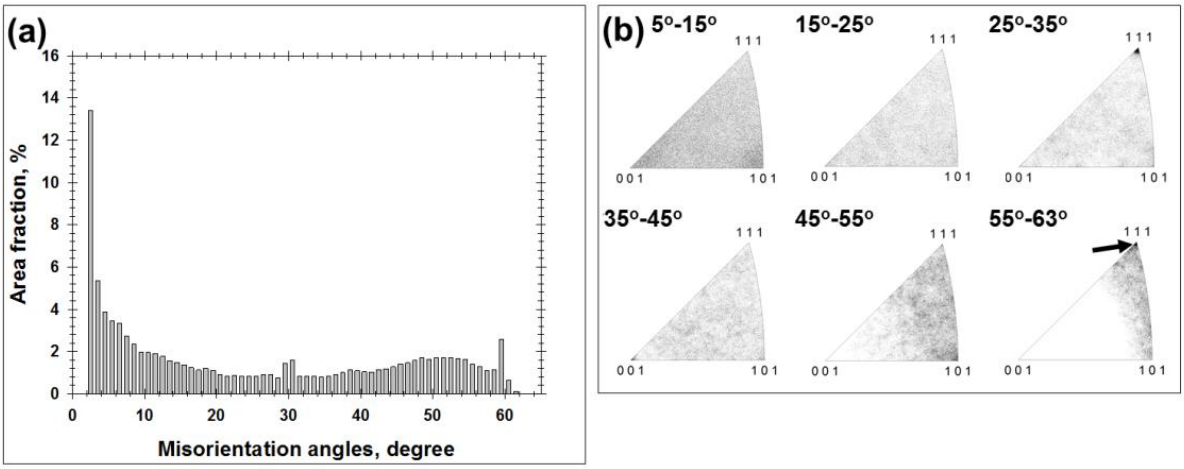


Fig. 6. (a) Misorientation distribution in δ-ferrite: (a) misorientation-angle distribution and (b) misorientation axis distribution. Arrows indicate crystallographic preference of 60°<111> misorientations

the pronounced LAB substructure within dendrites (Fig. 6(a)). On the other hand, a surprising result was an increased fraction of 60°<111> misorientations (Fig. 6). These boundaries are usually associated with twinning, but this mechanism in ferrite is only rarely observed in the scientific literature. Therefore, the subtle crystallographic preference of these misorientations was not clear.

Microstructure of austenite

The austenite phase is shown in Fig. 2(a). The grain-size distribution derived from the map is given in Fig. 4(b). The volume fraction of austenite was measured to be 4.1 %. This phase was arranged as the relatively fine-grained particles (Fig. 2(a,b)), which sometimes exhibited a lath-shaped morphology (Fig. 2(b). The latter observation was partially due to the precipitation of the austenitic phase at the grain boundaries of δ-ferrite (Fig. 2(b)).

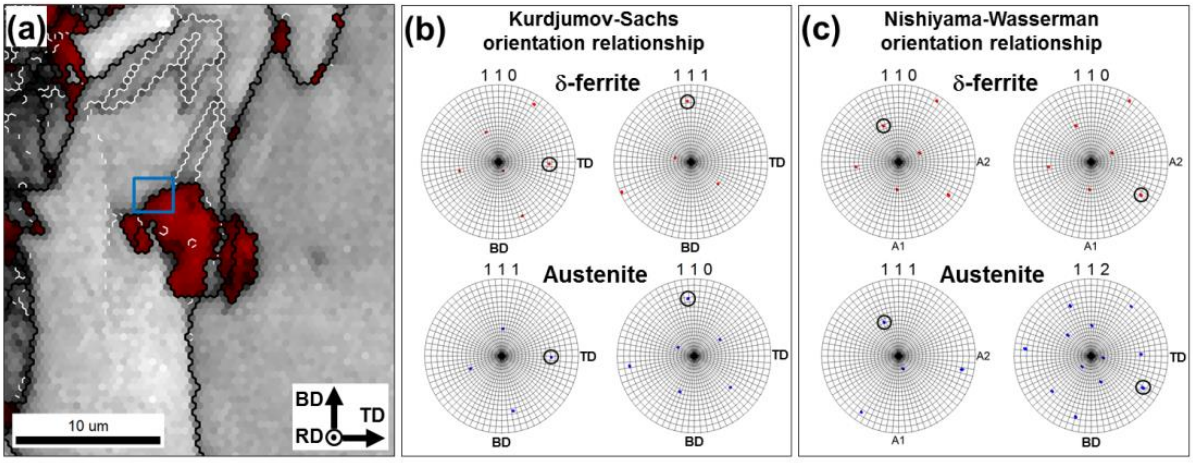


Fig. 7. Typical orientation relationship between δ-ferrite and austenite: (a) selected portion of EBSD image-quality map of microstructure (austenitic phase is highlighted with red) and pole figures showing the (b) Kurdjumov-Sachs relation and (c) Nishiyama-Wasserman relation. In (a), the selected area indicates the particular microstructural region from which orientation data were taken. In (b) and (c), the closest related directions in δ-ferrite and austenite are circled. BD, RD, and TD define the building direction, the motion direction of the powder roller, and the transverse direction, respectively

To evaluate a possible orientation relationship between austenite and δ-ferrite, the local orientations between the austenitic particles and the surrounding δ-ferrite matrix were compared, as exemplified in Fig. 7. Assuming either the Kurjumov-Sachs (K-S) $\{110\}_\delta$ // $\{111\}_\gamma$, $<111>_\delta$ // $<110>_\gamma$ or Nishiyama-Wasserman (N-W) $\{110\}_\delta$ // $\{111\}_\gamma$, $<110>_\delta$ // $<112>_\gamma$ relations between the phases, the appropriate pole figures were compared (Fig. 7(b,c)). For clarity, crystallographic directions in the austenite that are close to the δ-ferrite were circled. It is seen that the δ-ferrite-to-austenite phase transformation was governed by an orientation relationship, and it could be described in terms of both the K-S and N-W relations.

To provide a more statistically reliable insight into the orientation relationship between the δ-ferrite and austenite, misorientation across the phase boundaries was measured. Specifically, a particular orientation relationship can be expressed in terms of a particular misorientation [65,66]. Those were systematically measured and summarized as misorientation-angle and misorientation-axis distributions in Fig. 8, respectively. For clarity, the particular orientation relationships were indicated in the distributions.

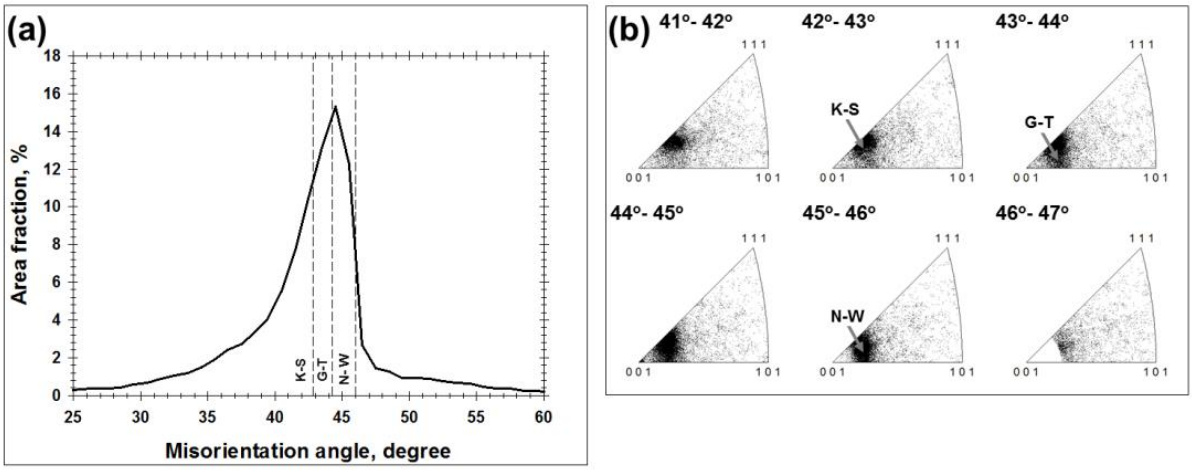


Fig. 8. Examination of orientation relationship between δ-ferrite and austenite using misorientations across the phase boundaries: (a) misorientation-angle distribution and (b) misorientation-axis distribution. The dotted lines in (a) and arrows in (b) indicate the approximate positions of the Kurdjumov-Sachs (K-S), Greniger-Trojano (G-T), and Nishiyama-Wasserman (N-W) orientation relationships

It is clear that the measured orientation relationships varied in the entire range from the K-S to N-W ones (Fig. 8), and the best fit was obtained with an "intermediate" Greniger-Trojano (G-T) relation (Fig. 8(a)). In *martensitic* structures, this effect is often reported in the scientific literature, being usually attributed to a relatively large orientation spread within the martensitic phase [67,68]. As follows from the present result (i.e., the *austenitic* structure), this phenomenon may be a characteristic of a displacive phase transformation in steels in general. Moreover, the revealed ambiguity may also be a result (at least partially) of a limited accuracy of EBSD in the determination of crystallographic axes (≈ 5°, according to Wilkinson [69]). Given the relatively small difference between the K-S and N-W relationships, the unbiased distinguishing between them using EBSD is challenging.

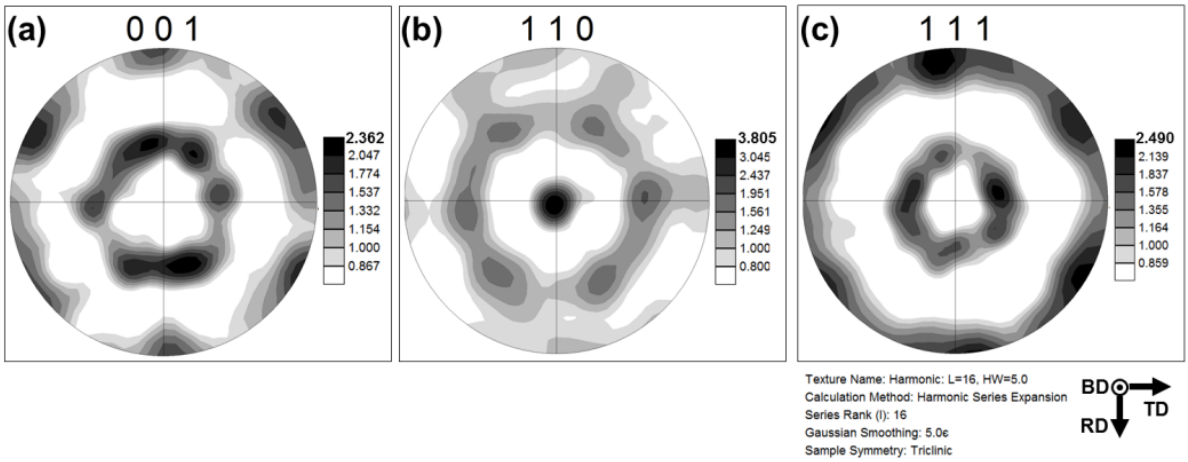


Fig. 9. Pole figures (a) 100, (b) 110, and (c) 111 showing the crystallographic texture in austenite. Note: The reference frame for all pole figures is given in the bottom right corner. BD, RD, and TD define the building direction, the motion direction of the powder roller, and the transverse direction, respectively

The orientation relationship between the phases implies a possibility of the formation of a transformation texture. To evaluate this potential effect, orientation data were extracted from the austenitic phase and arranged as 100, 110, and 111 pole figures in Fig. 9(a,b,c), respectively. The common reference frame for the pole figures was shown in the bottom right corner.

The distinct <110> fiber texture aligned with the building direction was revealed (Fig. 9(b)). In this context of particular interest was the broad similarity between the 110 and 111 pole figures in austenite (Fig. 9(b,c)) and the 111 and 110 pole figures in δ-ferrite (Fig. 5(b,c)). Accordingly, it was highly likely that the <110> fiber texture in austenite was inherited from the <111> fiber texture in δ-ferrite.

To provide further insight into microstructural processes within the austenitic phase, misorientation distribution was also examined (Fig. 10(a)). It was found that the characteristics of the distribution included a significant proportion of low-angle boundaries as well as a crystallographic preference of 60°<111> (or Σ3) misorientations (Fig. 10(a)).

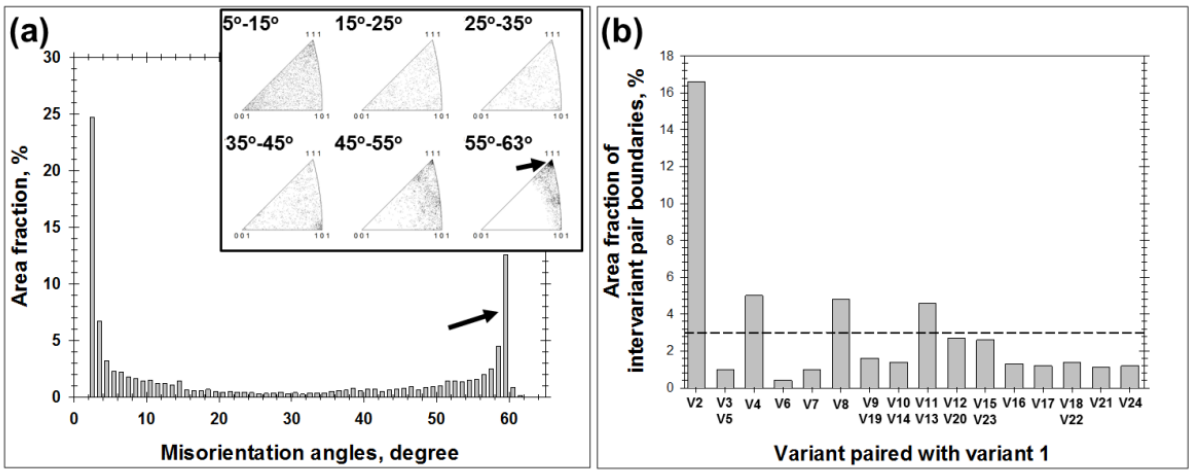


Fig. 10. (a) Misorientation distribution in austenite and (b) variant-pairing-frequency histogram derived from the austenitic phase assuming the K-S orientation relationship between δ-ferrite and austenite. In (a), misorientation-axis distribution is shown as an insert in the top right corner. In (b), the horizontal broken line represents the fraction of inter-variant misorientations assuming no variant selection

In austenite, the latter misorientations are typically associated with twinning. However, the activation of this mechanism is normally expected to operate during either plastic deformation or recrystallization/grain growth processes. Hence, a significant proportion of such boundaries in the L-PBFed microstructure was a non-trivial result.

Considering the orientation relationship between the austenite and δ-ferrite (Figs. 7 and 8), it is reasonable to hypothesize that the unusual character of the misorientation distribution may originate (at least partially) from the phase transformation. Due to the crystal symmetry of both phases, the multiple austenite variants of the orientation relationship may form within a particular parent δ-ferrite grain. Accordingly, the inter-variant boundaries may contribute to the unusual character of the misorientation distribution.

The inter-variant misorientations are often represented as those between the V1 variant and other variants [70]. Assuming the K-S orientation relationship between the δ-ferrite and austenite, the area fractions of the inter-variant boundaries were determined and summarized in Fig. 10(b). Because of crystallographic equivalency of some inter-variant misorientations (including V3/V5, V9/V19, V10/V14, V11/V13, V12/V20, V15/V23, and V18/V22 variant pairs), only 16 independent misorientations were measured, as indicated in Fig. 10(b).

The measurements revealed a distinct crystallographic preference of V1/V2 inter-variant boundaries (Fig. 10(b)), i.e., the 60° [11$\bar{1}$] misorientation [70]. This finding implied a strong variant selection that occurred during the δ-ferrite-to-austenite transformation. This phenomenon provided both the formation of the prominent transformation texture (Fig. 9(b)) and the crystallographic preference of the 60°<111> misorientations (Fig. 10(a)) in the austenitic phase.

The prevalence of the twin-related crystallographic variants during austenite reversion has also been reported by Nakada et al. [71]. This effect has been attributed to the significant residual stress in the parent martensitic phase [71]. Given the extremely high cooling rate, which is intrinsic to the L-PBF process, it is highly likely that the δ-ferrite in the present study was also characterized by considerable residual stress. Therefore, the concept proposed by Nakada et al. [71] explains well the pronounced variant selection during the δ-ferrite-to-austenite phase transformation.

Microstructure of martensite

The EBSD IQ map of martensitic phase is shown in Fig. 3(c). The grain-size distribution derived from the map is given in Fig. 4(c). The volume fraction of the martensite was measured to be 5.8 %. As follows from Fig. 3(c), the martensite particles were preferentially clustered in particular locations, which typically represented the triple joints of the local molten pools. In contrast to the austenitic phase, which often precipitated within the pools as grain-boundary particles, the martensite was rarely observed in such locations. This observation implied a relatively high stability of the grain-boundary austenite. Remarkably, the grain size of the martensite particles was comparable with that of the austenitic phase (Fig. 4(b,c)).

To investigate the potential orientation relationship between martensite and austenite, the local crystallographic orientations of several neighboring particles were

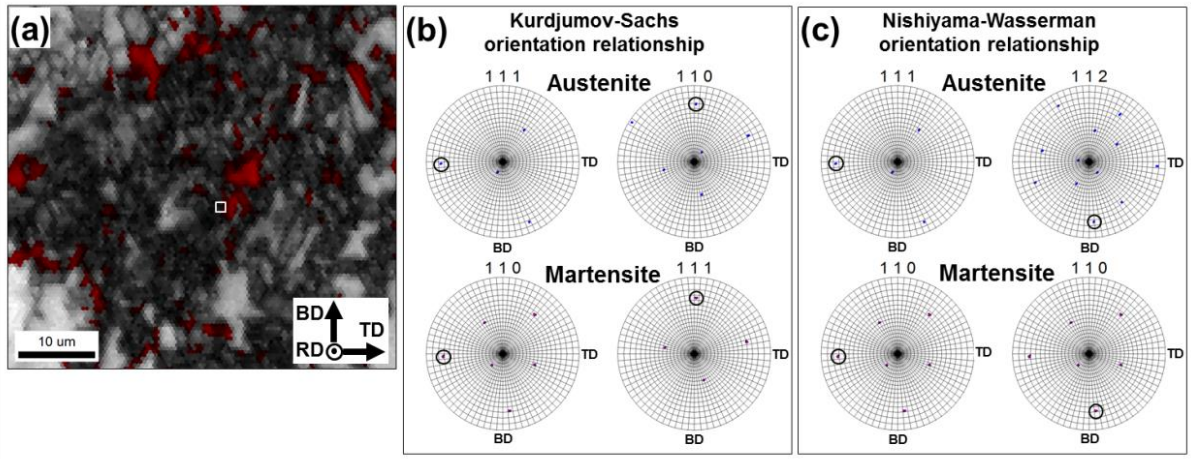


Fig. 11. Typical orientation relationship between austenite and martensite: (a) selected portion of EBSD image-quality map of microstructure (austenitic phase is highlighted with red) and pole figures showing the (b) Kurdjumov-Sachs relation and (c) Nishiyama-Wasserman relation. In (a), the selected area indicates the particular microstructural region from which orientation data were taken. In (b) and (c), the closest related directions in austenite and martensite are circled. BD, RD, and TD define the building direction, the motion direction of the powder roller, and the transverse direction, respectively

compared with each other, as exemplified in Fig. 11. It was found the phases were related through an orientation relationship, though it could not be unambiguously attributed to either the K-S or N-W one (Fig. 11(b,c)).

To provide a deeper inspection of this effect, the misorientations across the austenite/martensite phase boundaries were systematically measured, as shown in Fig. 12. By analogy with the austenitic transformation considered in the previous structure, the measured orientation relationships between the austenite and martensite varied in the entire range from the K-S to N-W (Fig. 12, and the best fit was again obtained with an "intermediate" Greniger-Trojano (G-T) relation (Fig. 12(a)). As noted above, this is a quite expectable result for martensitic structures that could be attributed to both the large orientation spread within the martensitic phase per se and the limited accuracy of the EBSD technique.

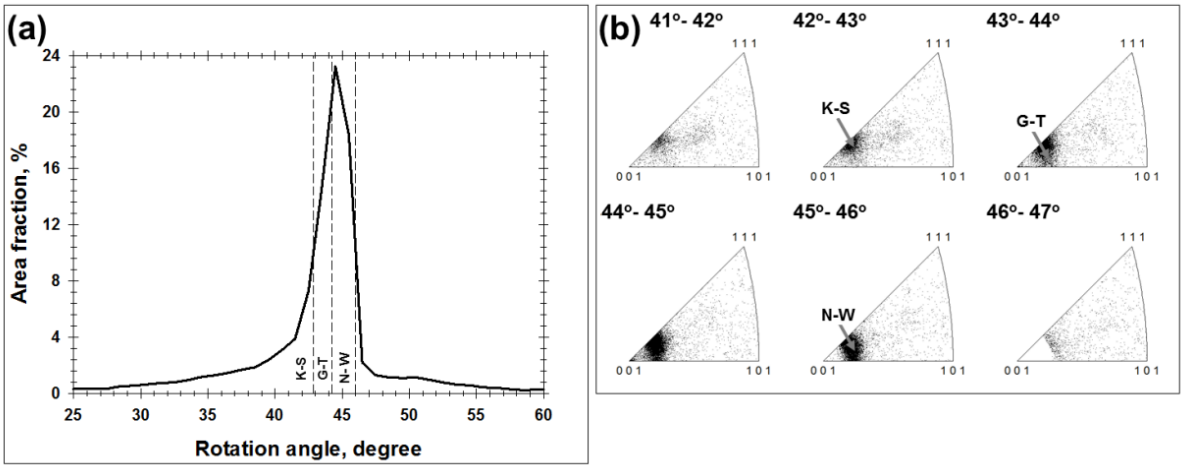


Fig. 12. Examination of orientation relationship between austenite and martensite using misorientations across the phase boundaries: (a) misorientation-angle distribution and (b) misorientation-axis distribution. The dotted lines in (a) and arrows in (b) indicate the approximate positions of the Kurdjumov-Sachs (K-S), Greniger-Trojano (G-T), and Nishiyama-Wasserman (N-W) orientation relationships

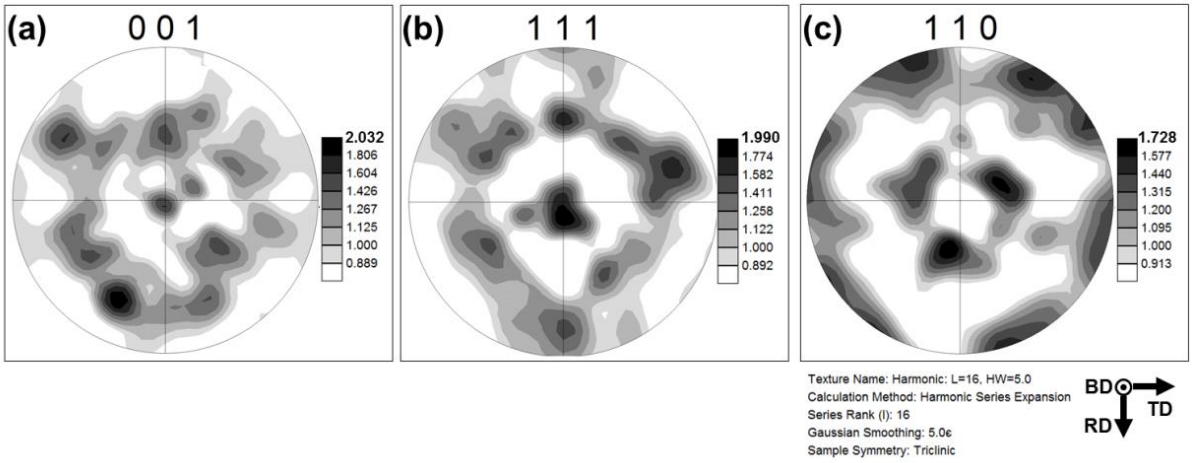


Fig. 13. Pole figures (a) 100, (b) 111, and (c) 110 showing crystallographic texture in martensite. Note: the reference frame for all pole figures is given in the bottom right corner. BD, RD, and TD define the building direction, the motion direction of the powder roller, and the transverse direction, respectively

The orientation relationship between the phases may result in a transformation texture during a phase transition. To check this possibility in the present case, the 100, 111, and 110 pole figures were calculated for the martensitic phase and summarized in Fig. 13(a,b,c), respectively. The broad similarity between the 111 and 110 pole figures in martensite (Fig. 13(b,c)) and the 110 and 111 pole figures in austenite (Fig. 9(b,c)) was found. Accordingly, a distinct <111>-fiber texture had developed in the martensitic phase (Fig. 13(b)).

Moreover, in the first approximation, the textural pattern in the martensite (Fig. 13) resembled that in δ-ferrite (Fig. 5). Hence, ignoring a significant reduction in texture intensity, the martensitic phase exhibited a "texture memory" effect. Hence, the textural pattern in the martensite could be described in terms of a poorly developed two-component <100> + <111> fiber texture (Fig. 13).

As mentioned above, an orientation relationship with a parent phase may exert a principal influence on misorientation distribution in a daughter phase. Indeed, the misorientation distribution in martensite showed a specific appearance (Fig. 14(a)),

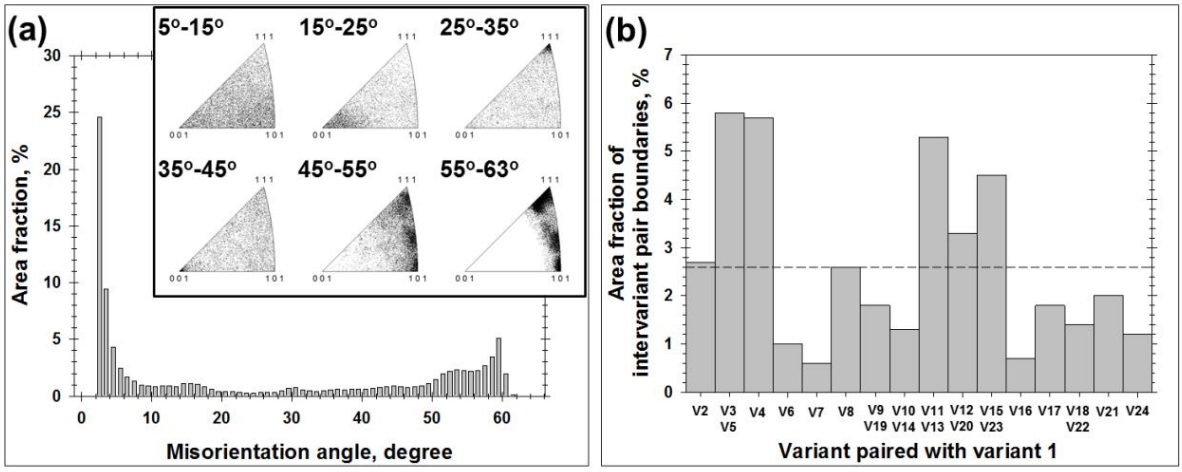


Fig. 14. (a) Misorientation distribution in martensite and (b) variant-pairing-frequency histogram derived from the martensitic phase assuming the K-S orientation relationship between the austenite and martensite. In (a), misorientation-axis distribution is shown as an insert in the top right corner. In (b), the horizontal broken line represents the fraction of inter-variant misorientations assuming no variant selection

which is typically reported for martensitic structures in the scientific literature [72–75]. Specifically, it included a prominent low-angle maximum and broad peak in the angular range of 50–60° as well as a pronounced clustering of the rotation axes of the 50–60° boundaries in-between <110>-<111> poles (Fig. 14(a)). This observation suggested that the misorientation distribution was dominated by the martensitic inter-variant boundaries.

To evaluate the variant selection that might occur during the martensitic transformation, the area fraction of the inter-variant boundaries between the V1 variant and other martensitic variants [76] was measured in Fig. 14(b). By analogy with the austenitic variants in Fig. 10(b), several inter-variant misorientations were combined together due to their crystallographic equivalency (Fig. 14(b)).

The obtained result evidenced that the variant selection during the martensitic transformation (Fig. 14(b)) was much less pronounced than that during the austenitic one (Fig. 10(b)). Nevertheless, the crystallographic preferences of V3/V5, V4, V11/V13, V15/V23, and V12/V20 variants were found.

Conclusions

This study was undertaken to evaluate the broad aspects of microstructural evolution during the L-PBF of 17-4 PH martensitic steel. To minimize retained porosity, the L-PBF was conducted under a relatively high volumetric energy density of 200 J/mm^3. To gain a thorough understanding of microstructural processes, an advanced EBSD technique was applied. The main conclusions derived from this work were as follows:

1. Quite expectedly, the L-PBF resulted in a distinct meso-scale structure, which consisted of an array of local molten pools. Given the fact that the depth of the pools was several times greater than the nominal thickness of the powder layer, it was suggested that the additive material experienced several melting-to-solidification cycles.
2. The evolved microstructure was dominated by δ-ferrite. This presumably indicated that the primary factor governing microstructure evolution during L-PBF was an extremely high cooling rate. Considering the development of a two-component <100> + <111> fiber texture in the δ-ferrite, it was concluded that this phase precipitated epitaxially at the bottom and side surfaces of the local molten pools and then preferentially grew along the building direction. The typical size of the δ-ferrite grains was comparable with that of the parent local molten pool, though the formation of a fine-grained layer along the pool borders was also sometimes revealed. The latter observation might be indicative of either the development of the chill zone at the solidification surface or the static recrystallization occurring in this region during thermal cycling. The δ-ferrite grains contained a developed LAB substructure, which presumably originated from the mutual impingement of the growing dendrites with close crystallographic orientations.
3. The austenitic phase preferentially nucleated at triple joints of the local molten pools. This observation suggested that the δ-ferrite-to-austenite phase transformation was mainly governed by the L-PBF thermal cycling. Additionally, the austenite precipitations were also observed within the pool area, along the δ-ferrite grain boundaries. The δ-ferrite-to-austenite phase transformation involved a strict selection of crystallographic variants, which, in turn, resulted in a distinct <111>-fiber transformation texture and the crystallographic preference of 60°<111> twin boundaries in the austenitic phase.

4. The martensitic transformation also preferentially occurred at the pool triple joints. Importantly, the martensitic phase exhibited a "texture memory" effect, i.e., the crystallographic texture in this phase was somewhat similar to that of the δ-ferrite. On the other hand, the much less pronounced variant selection during the martensitic transformation resulted in significant degradation of texture intensity.

CRediT authorship contribution statement

Ivan S. Nikitin: conceptualization, investigation, data curation, writing – review & editing; **E.A. Voropaeva**: investigation, writing – review & editing; **A.O. Semenyuk**: investigation, writing – review & editing; **R.S. Chernichenko**: investigation, writing – review & editing; **Pavel D. Dolzhenko**: investigation, writing – review & editing; **Sergei I. Borisov**: investigation, writing – review & editing; **Alexander A. Kalinenko**: investigation, writing – review & editing; **Elena V. Kaliuzhnaya**: writing – review & editing; **Ivan S. Zuiko**: investigation, writing – review & editing; **Lei Shi**: conceptualization, writing – review & editing; **Chuansong Wu**: conceptualization, writing – review & editing; **Sergei Yu. Mironov**: conceptualization, supervision, data curation, writing – original draft.

Conflict of interest

The authors declare that they have no conflict of interest.

References

1. Agarwala M, Bourell D, Beaman J, Marcus H, Barlow J. Direct selective laser sintering of metals. *Rapid Prototyping Journal*. 1995;1(1): 26–36.
2. Popovich AA, Sufiiarov VSh, Borisov EV, Polozov IA, Masaylo DV. Design and manufacturing of tailored microstructure with selective laser melting. *Materials Physics and Mechanics*. 2018;38(1): 1–10.
3. Vunnam S, Saboo A, Sudbrack C, Starr TL. Effect of powder chemical composition on the as-built microstructure of 17-4 PH stainless steel processed by selective laser melting. *Additive Manufacturing*. 2019;30: 100876.
4. Wang X, Liu Y, Shi T, Wang Y. Strain rate dependence of mechanical property in a selective laser melted 17-4 PH stainless steel with different states. *Materials Science and Engineering: A*. 2020;792: 139776.
5. Sabooni S, Chabok A, Feng SC, Blaauw H, Pijper TC, Yang HJ, Pei YT. Laser powder bed fusion of 17-4 PH stainless steel: A comparative study on the effect of heat treatment on the microstructure evolution and mechanical properties. *Additive Manufacturing*. 2021;46: 102176.
6. Kugelmeier CL, Unti LFK, Junior ELS, Souza NM, Jardini AL, Avila JA, Cintho OM, Zilnyk K. Microstructure evolution and corrosion resistance evaluation of 17-4 precipitation hardening stainless steel processed by laser powder bed fusion. *Journal of Materials Engineering and Performance*. 2025;34: 10537–10547.
7. Mazruee Sebdani R, Bilan HK, Gale JD, Wanni J, Madireddy G, Sealy MP, Achuthan A. Ultrasonic impact treatment (UIT) combined with powder bed fusion (PBF) process for precipitation hardened martensitic steels. *Additive Manufacturing*. 2024;84: 104078.
8. Hu Z, Zhu H, Zhang H, Zeng X. Experimental investigation on selective laser melting of 17-4PH stainless steel. *Optics & Laser Technology*. 2017;87: 17–25.
9. Yasa E, Atik I, Kandemir I. Material-specific phenomena and developing higher yield process parameters in laser powder bed fusion of 17-4 PH stainless steel. *Journal of the Brazilian Society of Mechanical Sciences and Engineering*. 2023;45: 38.
10. Murr LE, Gaytan SM, Ramirez DA, Martinez E, Hernandez J, Amato KN, Shindo PW, Medina FR, Wicker RB. Metal fabrication by additive manufacturing using laser and electron beam melting technologies. *Journal of Materials Science & Technology*. 2012;28(1): 1–14.

11. Yadollahi A, Shamsaei N, Thompson SM, Elwany A, Bian L. Effects of building orientation and heat treatment on fatigue behavior of selective laser melted 17-4 PH stainless steel. *International Journal of Fatigue*. 2017;94: 218–235.
12. Rafi HK, Pal D, Patil N, Starr TL, Stucker BE. Microstructure and mechanical behavior of 17-4 precipitation hardenable steel processed by selective laser melting. *Journal of Materials Engineering and Performance*. 2014;23: 4421–4428.
13. LeBrun T, Nakamoto T, Horikawa K, Kobayashi H. Effect of retained austenite on subsequent thermal processing and resultant mechanical properties of selective laser melted 17-4 PH stainless steel. *Materials & Design*. 2015;81: 44–53.
14. Rashid R, Masood SH, Ruan D, Palanisamy S, Rahman Rashid RA, Brandt M. Effect of scan strategy on density and metallurgical properties of 17-4PH parts printed by selective laser melting (SLM). *Journal of Materials Processing Technology*. 2017;249: 502–511.
15. Akita M, Uematsu Y, Kakiuchi T, Nakajima M, Kawaguchi R. Defect-dominated fatigue behavior in type 630 stainless steel fabricated by selective laser melting. *Materials Science and Engineering: A*. 2016;666: 19–26.
16. Ponnusamy P, Sharma B, Masood SH, Rahman Rashid RA, Rashid RR, Palanisamy S, Ruan D. A study of tensile behavior of SLM processed 17-4 PH stainless steel. *Materials Today: Proceedings*. 2021;45: 4531–4534.
17. Leo P, D'Ostuni S, Perulli PP, Sastre MAC, Fernandez-Abia AI, Barreiro J. Analysis of microstructure and defects in 17-4 PH stainless steel sample manufactured by selective laser melting. *Procedia Manufacturing*. 2019;41: 66–73.
18. Nezhadfar PD, Shrestha R, Phan N, Shamsaei N. Fatigue behavior of additively manufactured 17-4 PH stainless steel: Synergistic effects of surface roughness and heat treatment. *International Journal of Fatigue*. 2019;124: 188–204.
19. Nezhadfar PD, Burford E, Anderson-Wedge K, Zhang B, Shao S, Daniewicz SR, Shamsaei N. Fatigue crack growth behavior of additively manufactured 17-4 PH stainless steel: Effects of build orientation and microstructure. *International Journal of Fatigue*. 2019;123: 168–179.
20. Sun Y, Hebert RJ, Aindow M. Effect of laser scan length on the microstructure of additively manufactured 17-4PH stainless steel thin-walled parts. *Additive Manufacturing*. 2020;35: 101302.
21. Yadollahi A, Mahmoudi M, Elwany A, Doude H, Bian L, Newman JC. Effects of crack orientation and heat treatment on fatigue-crack-growth behavior of AM 17-4 PH stainless steel. *Engineering Fracture Mechanics*. 2020;226: 106874.
22. Aripin MA, Sajuri Z, Syarif J, Baghdadi AH, Mohamed IF. Evaluation of microstructure and porosity for 3D printed stainless steel. *Materials Today: Proceedings*. 2022;66(5): 3082–3086.
23. Sun Y, Hebert RJ, Aindow M. Effect of heat treatments on microstructural evolution of additively manufactured and wrought 17-4PH stainless steel. *Materials & Design*. 2018;156: 429–440.
24. Pasebani S, Ghayoor M, Badwe S, Irrinki H, Atre SV. Effects of atomizing media and post processing on mechanical properties of 17-4 PH stainless steel manufactured via selective laser melting. *Additive Manufacturing*. 2018;22: 127–137.
25. Hsu T-H, Chang Y-J, Huang C-Y, Yen H-W, Chen C-P, Jen K-K, Yeh A-C. Microstructure and property of a selective laser melting process induced oxide dispersion strengthened 17-4 PH stainless steel. *Journal of Alloys and Compounds*. 2019;803: 30–41.
26. Lee HJ, Dao VH, Ma YW, Yu JM, Yoon KB. Effects of process parameters on the high temperature strength of 17-4PH stainless steel produced by selective laser melting. *Journal of Mechanical Science and Technology*. 2020;34: 3261–3272.
27. Facchini L, Vicente N, Lonardelli I, Magalini E, Robotti P, Molinari A. Metastable austenite in 17-4 precipitation-hardening stainless steel produced by selective laser melting. *Advanced Engineering Materials*. 2010;12: 184–188.
28. Yadollahi A, Shamsaei N, Thompson SM, Elwany A, Bian L. Effects of building orientation and heat treatment on fatigue behavior of selective laser melted 17-4 PH stainless steel. *International Journal of Fatigue*. 2017;94: 218–235.
29. LeBrun T, Tanigaki K, Horikawa K, Kobayashi H. Strain rate sensitivity and mechanical anisotropy of selective laser melted 17-4 PH stainless steel. *Mechanical Engineering Journal*. 2014;1: SMM0049.
30. Kokosza A, Pacyna J. Evaluation of retained austenite stability in heat treated cold work tool steel. *Journal of Materials Processing Technology*. 2005;162–163: 327–331.
31. Fields B, Amiri M, Lim J, Purstl JT, Begley MR, Apelian D, Valdevit L. Microstructural control of a multi-phase PH steel printed with laser powder bed fusion. *Advanced Materials Technologies*. 2024;9: 2301037.
32. Vysotskiy I, Malopheyev S, Zuiko I, Mironov S, Kaibyshev R. Crystallographic aspects of 17-4 PH martensitic steel produced by laser-powder bed fusion. *Materials Characterization*. 2022;194: 112405.
33. Vysotskiy I, Malopheyev S, Zuiko I, Mironov S, Kaibyshev R. Microstructure distribution in 17-4 PH martensitic steel produced by selective laser melting. *Metallurgical and Materials Transactions A*. 2022;53: 4143–4147.

34. Zai L, Zhang C, Wang Y, Guo W, Wellmann D, Tong X, Tian Y. Laser powder bed fusion of precipitation-hardened martensitic stainless steels: A review. *Metals*. 2020;10: 255–280.
35. Alnajjar M, Christien F, Wolski K, Bosch C. Evidence of austenite by-passing in a stainless steel obtained from laser melting additive manufacturing. *Additive Manufacturing*. 2019;25: 187–195.
36. Alnajjar M, Christien F, Bosch C, Wolski K. A comparative study of microstructure and hydrogen embrittlement of selective laser melted and wrought 17-4 PH stainless steel. *Materials Science and Engineering: A*. 2020;785: 139363.
37. Moyle MS, Haghdadi N, Liao XZ, Ringer SP, Primig S. On the microstructure and texture evolution in 17-4 PH stainless steel during laser powder bed fusion: Towards textural design. *Journal of Materials Science & Technology*. 2022;117: 183–195.
38. Haines MP, Moyle MS, Rielli VV, Haghdadi N, Primig S. Site-specific Cu clustering and precipitation in laser powder-bed fusion 17-4 PH stainless steel. *Scripta Materialia*. 2024;241: 115891.
39. Haines MP, Moyle MS, Rielli VV, Luzin V, Haghdadi N, Primig S. Experimental and computational analysis of site-specific formation of phases in laser powder bed fusion 17-4 precipitate hardened stainless steel. *Additive Manufacturing*. 2023;73: 103686.
40. Yeon S-M, Yoon J, Kim TB, Lee SH, Jun T-S, Son Y, Choi K. Normalizing effect of heat treatment processing on 17-4 PH stainless steel manufactured by powder bed fusion. *Metals*. 2022;12: 704.
41. Lashgari HR, Kong C, Adabifiroozjaei E, Li S. Microstructure, post thermal treatment response, and tribological properties of 3D printed 17-4 PH stainless steel. *Wear*. 2020;456–457: 203367.
42. Moyle MS, Haghdadi N, Theska F, Haines MP, Liao XZ, Ringer SP, Primig S. Effect of compositional variations on the heat treatment response in 17-4 PH stainless steel fabricated by laser powder bed fusion. *Materials Characterization*. 2024;209: 113768.
43. Moyle MS, Haghdadi N, Luzin V, Salvemini F, Liao XZ, Ringer SP, Primig S. Correlation of microstructure, mechanical properties, and residual stress of 17-4 PH stainless steel fabricated by laser powder bed fusion. *Journal of Materials Science & Technology*. 2024;198: 83–97.
44. Zhao D, Guo Y, Lai R, Wen Y, Wang P, Liu C, Chen Z, Yang C, Li S, Chen W, Liu Z. Abnormal three-stage plastic deformation in a 17-4 PH stainless steel fabricated by laser powder bed fusion. *Materials Science and Engineering: A*. 2022;858: 144160.
45. Nezhadfar PD, Anderson-Wedge K, Daniewicz SR, Phan N, Shao S, Shamsaei N. Improved high cycle fatigue performance of additively manufactured 17-4 PH stainless steel via in-process refining micro-/defect-structure. *Additive Manufacturing*. 2020;36: 101604.
46. Singh KK, Moridi A. Metastability mediated grain size control in PH 17-4 stainless steel fabricated using laser-powder bed fusion (LPBF). *Materialia*. 2023;30: 101857.
47. Weaver JS, Whiting J, Tondare V, Beauchamp C, Peltz M, Tarr J, Phan TQ, Donmez MA. The effects of particle size distribution on the rheological properties of the powder and the mechanical properties of additively manufactured 17-4 PH stainless steel. *Additive Manufacturing*. 2021;39: 101851.
48. Murr LE, Martinez E, Hernandez J, Collins S, Amato KN, Gaytan SM, Shindo PW. Microstructures and properties of 17-4 PH stainless steel fabricated by selective laser melting. *Journal of Materials Research and Technology*. 2012;1: 167–177.
49. Herzog D, Seyda V, Wycisk E, Emmelmann C. Additive manufacturing of metals. *Acta Materialia*. 2016;117: 371–392.
50. Murr LE, Martinez E, Amato KN, Gaytan SM, Hernandez J, Ramirez DA, Shindo PW, Medina F, Wicker RB. Fabrication of metal and alloy components by additive manufacturing: Examples of 3D materials science. *Journal of Materials Research and Technology*. 2012;1: 42–54.
51. Sabzi HE, Lim S-H, Crociata DD, Castellote-Alvarez R, Simonelli M, San-Martin D, Hao X, Choi P-P, Rivera-Diaz-del-Castillo PEJ. Genetic design of precipitation-hardening stainless steels for additive manufacturing. *Acta Materialia*. 2024;274: 120018.
52. Brown B, Newkirk J, Liou F. Absorption of nitrogen during pulsed wave L-PBF of 17-4 PH steel. *Materials*. 2021;14: 560.
53. Humphreys FJ. Quantitative metallography by electron backscattered diffraction. *Journal of Microscopy*. 1999;195: 170–185.
54. Mahmoodkhani Y, Ali U, Shahabad SI, Kasinathan AR, Esmaeilizadeh R, Keshavarzkermani A, Marzbanrad E, Toyserkani E. On the measurement of effective powder layer thickness in laser powder-bed fusion additive manufacturing of metals. *Progress in Additive Manufacturing*. 2019;4: 109–116.
55. Wilson AW, Madison JD, Spanos G. Determining phase volume fraction in steels by electron backscattered diffraction. *Scripta Materialia*. 2001;45: 1335–1340.

56. Wu J, Wray PJ, Garcia CI, Hua M, Deardo AJ. Image quality analysis: A new method of characterizing microstructures. *ISIJ International*. 2005;45: 254–262.
57. Calcagnotto M, Ponge D, Raabe D. Microstructure control during fabrication of ultrafine grained dual-phase steel: Characterization and effect of intercritical annealing parameters. *ISIJ International*. 2012;52: 874–883.
58. Kang JY, Park SJ, Moon MB. Phase analysis on dual-phase steel using band slope of electron backscatter diffraction pattern. *Microscopy and Microanalysis*. 2013;19: 13–16.
59. Im Y-R, Kim E-Y, Song T, Lee JS, Suh D-W. Tensile properties and stretch-flangeability of TRIP steels produced by quenching and partitioning (Q&P) process with different fractions of constituent phases. *ISIJ International*. 2021;61: 572–581.
60. Shen C, Wang C, Huang M, Xu N, Zwaag S, Xu W. A generic high-throughput microstructure classification and quantification method for regular SEM images of complex steel microstructures combining EBSD labeling and deep learning. *Journal of Materials Science & Technology*. 2021;93: 191–204.
61. Ostromujof TM, Purohit RRPP, Breumier S, Gey N, Salib M, Germain L. Deep learning for automated phase segmentation in EBSD maps. A case study in dual phase steel microstructures. *Materials Characterization*. 2022;184: 111638.
62. Kang JY. Qualities of electron backscatter diffraction patterns and image contrast from a ferritic-martensitic steel microstructure. *Materials Characterization*. 2022;187: 111826.
63. Kozlowska A, Radwanski K, Grajcar A. Identification of structural constituents in advanced multiphase high-strength steels using electron back-scattered diffraction. *Symmetry*. 2024;16: 1630.
64. Pirgazi H, Sanjari M, Tamimi S, Amirkhiz BS, Kestens LAI, Mohammadi M. Texture evolution in selective laser melted maraging stainless steel CX with martensitic transformation. *Journal of Materials Science*. 2021;56: 844–853.
65. Sato H, Zaefferer S. A study on the formation mechanisms of butterfly-type martensite in Fe–30% Ni alloy using EBSD-based orientation microscopy. *Acta Materialia*. 2009;57(6): 1931–1937.
66. Zaefferer S, Elhami NN, Konijnenberg P. Electron backscatter diffraction (EBSD) techniques for studying phase transformations in steels. In: Pereloma E, Edmonds DV. (Eds) *Phase Transformations in Steels*. Woodhead Publishing; 2012. p.557–587.
67. Shibata A, Morito S, Furuhara T, Maki T. Local orientation change inside lenticular martensite plate in Fe–33Ni alloy. *Scripta Materialia*. 2005;53(5): 597–602.
68. Zisman AA, Zolotorevsky NYu, Petrov SN, Khlusova EI, Yashina EA. Panoramic crystallographic analysis of structure evolution in low-carbon martensitic steel under tempering. *Metal Science and Heat Treatment*. 2018;60(3–4): 142–149.
69. Wilkinson AJ. A new method for determining small misorientations from electron back scatter diffraction patterns. *Scripta Materialia*. 2001;44: 2379–2385.
70. Haghdadi N, Cizek P, Hodgson PD, Tari V, Rohrer GS, Beladi H. Effect of ferrite-to-austenite phase transformation path on the interface crystallographic character distributions in a duplex stainless steel. *Acta Materialia*. 2018;145: 196–209.
71. Nakada N, Tsuchiyama T, Takaki S, Hashizume S. Variant selection of reversed austenite in lath martensite. *ISIJ International*. 2007;47(10): 1527–1532.
72. Stormvinter A, Mitsche S, Cerjak H. Martensite laths in creep resistant martensitic 9-12% Cr steels: calculation and measurement of misorientations. *Materials Characterization*. 2007;58: 874–882.
73. Kim JH, Miyamoto G, Shibata A, Hojo T, Koyama M, Zhang Y, Furuhara T. Influence of austenite grain boundary misorientation on hydrogen-induced intergranular crack propagation in a medium carbon martensitic steel. *Acta Materialia*. 2024;274: 120036.
74. Sun H, Shao M, Lu N, Li X, Li L, Wang Z, Jiang J, Zhang H. The morphology and crystallography of lath martensite via high pressure martensitic transformation in Fe-0.45 wt.% C steel. *Acta Materialia*. 2025;284: 120624.
75. Aletdinov AF, Mironov SYu, Korznikova GF, Zaripova ZG, Konkova TN, Myshlyayev MM. EBSD analiz mikrostruktury austenitnoy stali posle prokatki v kriogennykh usloviyakh. *Materials Physics and Mechanics*. 2017;33: 29–40. (In Russian).
76. Stormvinter A, Miyamoto G, Furuhara T, Hedstrom P, Borgenstam A. Effect of carbon content on variant pairing of martensite in Fe-C alloys. *Acta Materialia*. 2012;60: 7265–7274.